JAAS

Accepted Manuscript

This is an *Accepted Manuscript*, which has been through the Royal Society of Chemistry peer review process and has been accepted for publication.

Accepted Manuscripts are published online shortly after acceptance, before technical editing, formatting and proof reading. Using this free service, authors can make their results available to the community, in citable form, before we publish the edited article. We will replace this *Accepted Manuscript* with the edited and formatted *Advance Article* as soon as it is available.

You can find more information about *Accepted Manuscripts* in the Information for Authors.

Please note that technical editing may introduce minor changes to the text and/or graphics, which may alter content. The journal's standard Terms & Conditions and the Ethical guidelines still apply. In no event shall the Royal Society of Chemistry be held responsible for any errors or omissions in this *Accepted Manuscript* or any consequences arising from the use of any information it contains.

ROYAL SOCIETY OF CHEMISTRY

www.rsc.org/jaas

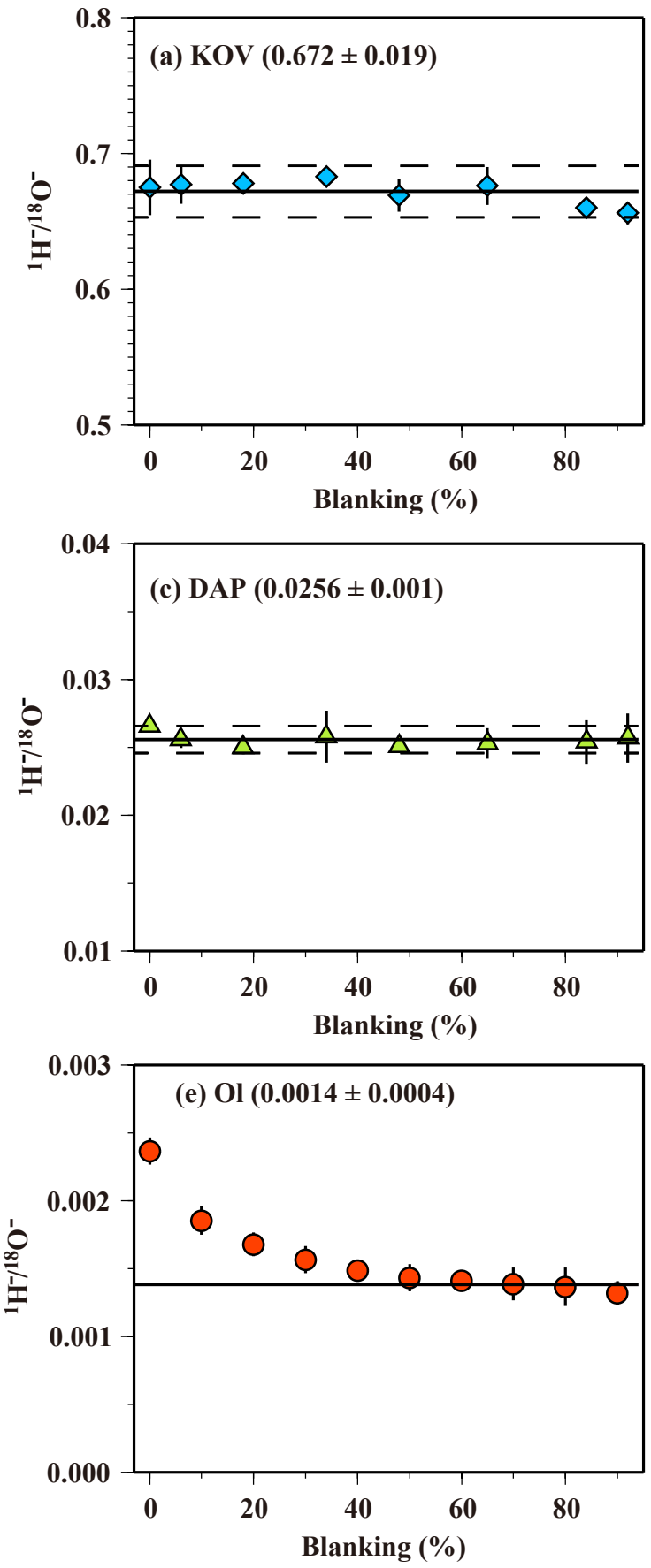

Fig. 1

Hu et al., 2014

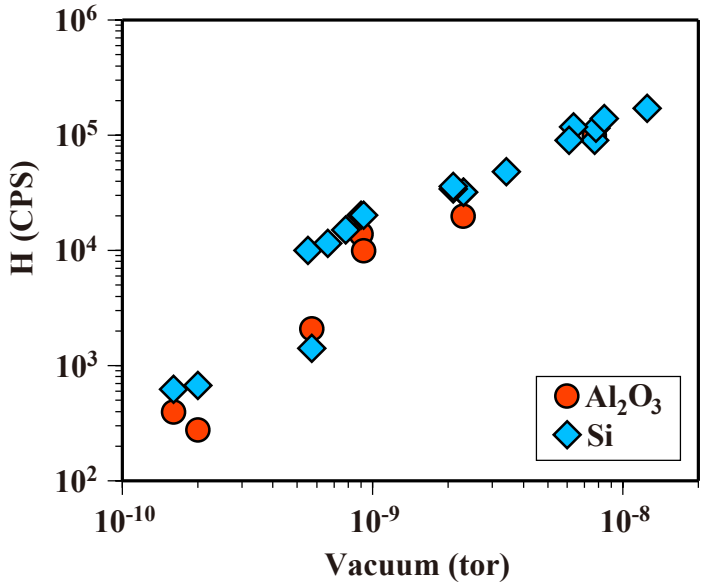

Fig. 2 Hu et al., 2014

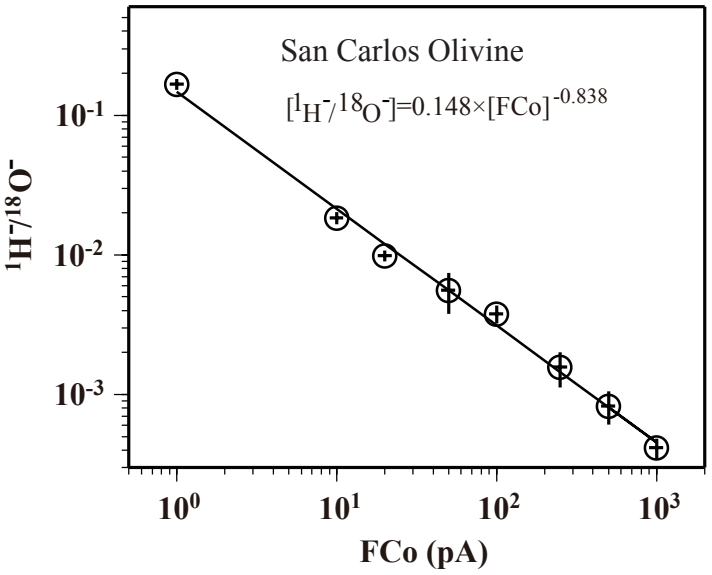

Fig. 3 Hu et al., 2014

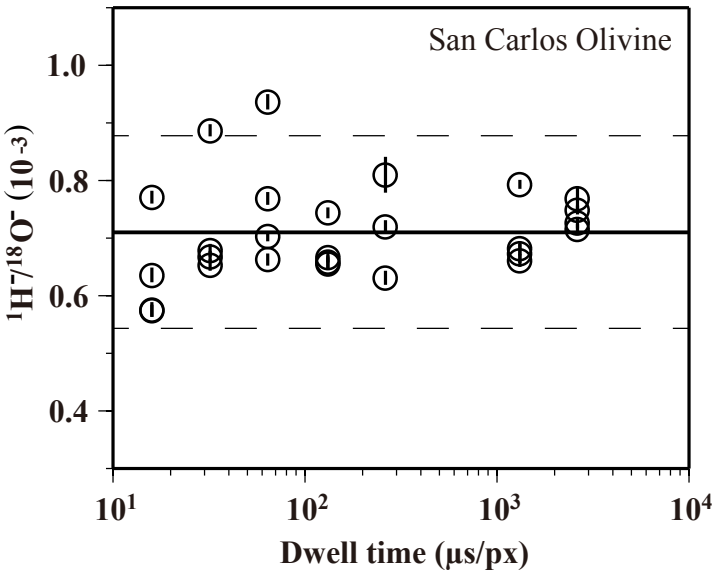

Fig. 4 Hu et al., 2014

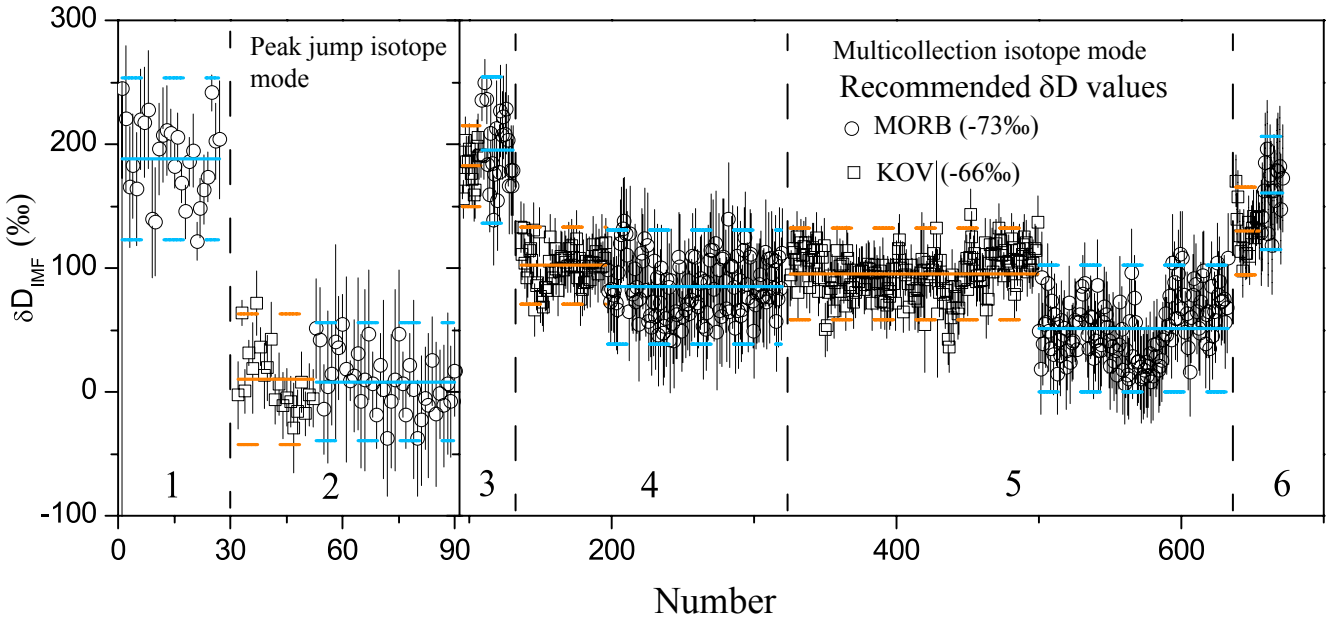

Fig. 5 Hu et al., 2014

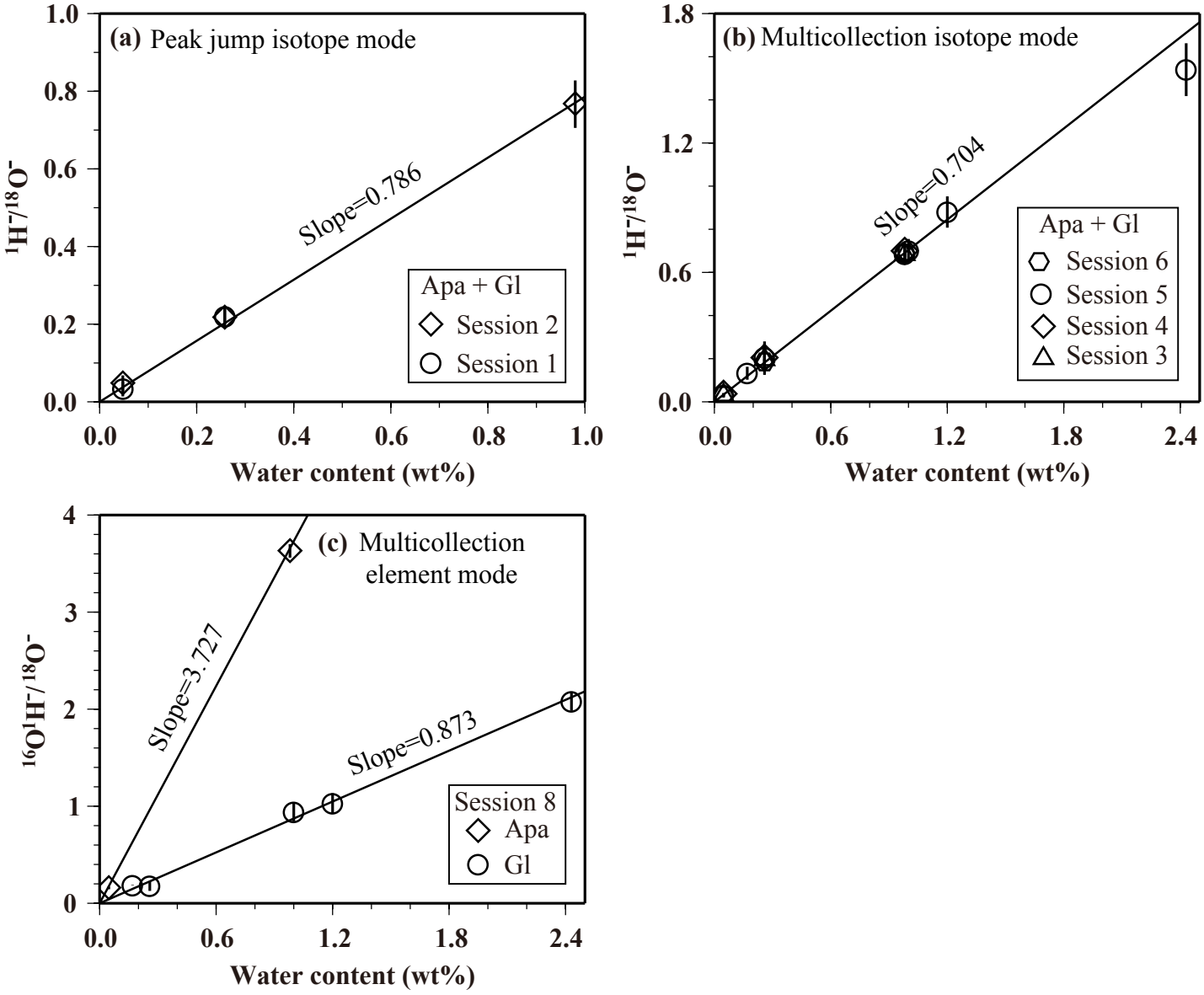

Fig. 6

Hu et al., 2014

Tables 1-11

Table 1. Water contents and δD values of apatite and silicate glass standards used in this work.

Sample	H_2O (wt%)	δD* ‰	Description	References
KOV	0.98	-66±21	Kovdor apatite, Russia	[17]
DAP	0.0478	-120±5	Durango apatite, Mexico	[9]
MORB	0.258	-73±2	Basaltic glass	Personal communication
1833-1	2.43		Basaltic glass, synthetic	[6, 18]
1833-11	1.20		Basaltic glass, synthetic	[6, 18]
519-4-1	0.17		Basaltic glass, synthetic	[6, 19]
ND 70-01	1.0		Basaltic glass, synthetic	Personal communication
Ol	<0.001		San Carlos olivine, U.S.A	[20]

* Average ± 2SD, $\delta D=((D/H)_{sample}/(D/H_{SMOW})-1)\times 1000$, where SMOW is the standard mean ocean water with the D/H ratio of 1.5576×10^{-4} [21].

Table 2. Detector setup of NanoSIMS 50L.

Mode	BF	EM#1	EM#2	EM#3	EM#4	EM#5	EM#6	EM#7
1		$^{1}H^{-}$	$^{2}D^{-}$		$^{12}C^{-}$			$^{18}O^{-}$
2	B1	$^{1}H^{-}$	$^{2}D^{-}$			$^{12}C^{-}$		
	B2			$^{18}O^{-}$				
3			$^{16}O^{1}H^{-}$	$^{18}O^{-}$				

BF: magnetic field was switched between B1 and B2.

Mode: 1—multicollection isotope mode; 2—peak jump isotope mode; 3—multicollection element mode.

Table 3. Measurements of the standards with various blanking percents.

Sample	Blanking %	$^{1}H^{-}/^{18}O^{-}$ [a]	2SD [b]	$^{2}D^{-}/^{1}H^{-}$ [a]	2SD [b]	$^{12}C^{-}/^{18}O^{-}$	2SD [a]
DAP	92	2.57E-02	1.81E-03	1.61E-04	6.12E-05	2.09E-04	3.06E-04
	84	2.54E-02	1.59E-03	1.79E-04	3.37E-05	1.37E-04	3.50E-05
	65	2.53E-02	1.12E-03	1.74E-04	2.91E-05	1.67E-04	7.12E-05
	48	2.51E-02	4.68E-04	1.77E-04	2.10E-05	2.16E-04	1.35E-04
	34	2.58E-02	1.92E-03	1.66E-04	2.42E-05	2.38E-04	6.67E-05
	18	2.50E-02	4.90E-04	1.77E-04	1.55E-05	3.45E-04	1.03E-04
	6	2.56E-02	6.32E-04	1.72E-04	7.70E-06	4.80E-04	3.88E-05
	0	2.66E-02	3.55E-04	1.64E-04	1.32E-05	1.90E-03	4.31E-03
KOV	92	6.56E-01	8.06E-03	1.64E-04	1.75E-05	6.08E-02	8.52E-04
	84	6.60E-01	4.14E-03	1.58E-04	6.81E-06	6.17E-02	1.07E-02
	65	6.76E-01	1.41E-02	1.57E-04	1.41E-06	5.81E-02	5.83E-03
	48	6.69E-01	1.21E-02	1.62E-04	3.19E-06	6.59E-02	2.37E-02
	34	6.83E-01	3.39E-03	1.58E-04	4.19E-06	6.07E-02	9.18E-03
	18	6.78E-01	4.81E-03	1.58E-04	4.40E-06	6.51E-02	6.04E-03
	6	6.77E-01	1.41E-02	1.60E-04	2.36E-06	7.01E-02	2.56E-02
	0	6.75E-01	2.06E-02	1.59E-04	2.02E-06	6.92E-02	8.52E-04
Ol	0	2.37E-03	1.00E-04			2.73E-04	1.01E-05
	11	1.86E-03	1.05E-04			2.14E-04	7.03E-06
	20	1.68E-03	8.82E-05			1.93E-04	6.47E-06
	30	1.57E-03	1.00E-04			1.79E-04	6.13E-06
	40	1.49E-03	6.67E-05			1.70E-04	5.84E-06
	50	1.43E-03	1.00E-04			1.63E-04	5.67E-06
	60	1.41E-03	6.67E-05			1.58E-04	4.93E-06
	70	1.39E-03	1.20E-04			1.54E-04	4.79E-06
	80	1.37E-03	1.41E-04			1.52E-04	5.62E-06
	90	1.32E-03	8.82E-05			1.50E-04	6.55E-06

[a]Average of the analyses;

[b]Standard deviation.

Table 4. $^{1}H^{-}$ counting rate of anhydrous silicon wafer and sapphire under various conditions of vacuum in the analysis chamber.

Sample	Vaccum (tor)	$^{1}H^{-}$ (cps)	Sample	Vaccum (tor)	$^{1}H^{-}$ (cps)
Si wafer	9.00E-10	2.00E+04	Al_2O_3	2.00E-10	2.80E+02
	9.20E-10	2.00E+04		1.60E-10	4.00E+02
	7.80E-10	1.50E+04		2.30E-09	2.00E+04
	5.50E-10	1.00E+04		5.70E-10	2.10E+03
	6.60E-10	1.15E+04		7.70E-09	1.00E+05
	2.00E-10	6.70E+02		9.00E-10	1.40E+04
	1.60E-10	6.20E+02		9.20E-10	1.00E+04
	2.30E-09	3.20E+04			
	2.30E-09	3.20E+04			
	5.70E-10	1.40E+03			
	7.70E-09	9.00E+04			
	7.80E-09	1.15E+05			
	2.10E-09	3.41E+04			
	1.25E-08	1.71E+05			
	8.42E-09	1.38E+05			
	6.33E-09	1.18E+05			
	2.10E-09	3.60E+04			
	3.42E-09	4.80E+04			
	6.10E-09	8.95E+04			

Table 5. Measurements of San Carlos olivine with various primary beam current.

FC_o* (pA)	$^{1}H^{-}/^{18}O^{-}$	2SD[a]	$^{12}C^{-}/^{18}O^{-}$	2SD[a]
1	1.67E-01	1.49E-02	4.56E-02	5.18E-03
10	1.84E-02	1.84E-03	9.52E-03	2.71E-03
20	9.91E-03	8.87E-04	3.81E-03	4.61E-04
50	5.61E-03	1.84E-03	3.66E-03	2.14E-03
100	3.78E-03	5.41E-04	1.28E-03	3.14E-04
250	1.57E-03	4.46E-04	5.60E-04	1.73E-04
500	8.29E-04	2.23E-04	5.28E-04	2.12E-04
1000	4.14E-04	6.96E-05	6.71E-04	1.65E-04

*Primary beam current;

[a]Standard deviation;

Table 6. Measurements of San Carlos olivine with different dwell time.

Dwell time* (μs/pixel)	$^{1}H^{-}/^{18}O^{-}$	$2\sigma^{a}$	$^{12}C^{-}/^{18}O^{-}$	$2\sigma^{a}$
16	5.76E-04	1.25E-05	2.95E-04	6.62E-06
16	6.36E-04	1.32E-05	3.25E-04	8.57E-06
16	7.71E-04	1.14E-05	3.82E-04	9.77E-06
16	5.74E-04	1.04E-05	3.81E-04	8.77E-06
Average	*6.39E-04*	*1.85E-04*	*3.46E-04*	*8.58E-05*
32	8.87E-04	1.03E-05	1.00E-03	1.84E-05
32	6.68E-04	1.00E-05	4.83E-04	1.17E-05
32	6.53E-04	1.00E-05	4.13E-04	1.17E-05
32	6.79E-04	1.14E-05	4.29E-04	1.19E-05
Average	*7.22E-04*	*2.21E-04*	*5.82E-04*	*5.65E-04*
64	7.03E-04	8.82E-06	4.58E-04	1.08E-05
64	6.63E-04	1.04E-05	4.37E-04	9.70E-06
64	7.69E-04	1.12E-05	4.52E-04	1.06E-05
64	9.37E-04	1.33E-05	7.35E-04	1.46E-05
Average	*7.68E-04*	*2.42E-04*	*5.20E-04*	*2.86E-04*
132	6.56E-04	1.08E-05	3.68E-04	8.03E-06
132	6.67E-04	9.58E-06	4.22E-04	8.53E-06
132	6.59E-04	1.14E-05	4.27E-04	1.05E-05
132	7.44E-04	9.06E-06	4.51E-04	1.09E-05
Average	*6.82E-04*	*8.34E-05*	*4.17E-04*	*7.03E-05*
264	6.31E-04	1.19E-05	2.97E-04	7.36E-06
264	7.20E-04	1.09E-05	4.74E-04	1.26E-05
264	8.10E-04	3.15E-05	3.89E-04	8.72E-06
Average	*7.20E-04*	*1.80E-04*	*3.87E-04*	*1.77E-04*
1320	6.61E-04	1.15E-05	3.72E-04	9.45E-06
1320	6.73E-04	1.66E-05	4.06E-04	9.11E-06
1320	6.82E-04	1.25E-05	4.41E-04	1.09E-05
1320	7.93E-04	7.75E-06	7.71E-04	1.37E-05
Average	*7.02E-04*	*1.22E-04*	*4.98E-04*	*3.69E-04*
2640	7.49E-04	7.42E-06	5.44E-04	8.46E-06
2640	7.16E-04	8.56E-06	4.56E-04	7.52E-06
2640	7.27E-04	9.87E-06	4.08E-04	8.06E-06

2640	7.69E-04	1.95E-05	4.80E-04	7.89E-06
Average	*7.40E-04*	*4.65E-05*	*4.72E-04*	*1.14E-04*

[*]The total counting time of each analysis was kept to a same value (104.8 s) by adjusting cycle numbers;

[a]Standard error of analysis;

Italic *Average* with standard deviation.

Table 7. Instrumental mass fractionation (IMF) and hydrogen isotope correction coefficient (α_{IMF}) of MORB glass and Kovdor apatite.

		MORB				KOV			
Session*	Date	n	IMF (‰)	2σ[a](‰)	α_{IMF}[b]	n	IMF (‰)	2σ[a] (‰)	α_{IMF}[b]
1	Apr, 2011	29	188	66	1.188				
2	Oct, 2011	38	8	48	1.008	21	10	38	1.010
3	Apr, 2012	23	195	59	1.195	14	182	33	1.182
4	Dec, 2012	124	85	46	1.085	61	102	31	1.102
5	Sep, 2013	134	51	51	1.051	175	96	37	1.096
6	Apr, 2014	16	161	45	1.161	18	130	36	1.130

*Analytical sessions 1 and 2 were carried out in peak jump isotope mode and sessions 3-6 in multicollection isotope mode;

n: Analysis numbers;

IMF=$1000\times[D/H_m/D/H_r-1]$, where D/H_m is the measured value and D/H_r is the recommended value;

[a]Standard deviation.

[b]Hydrogen isotope correction coefficient, $\alpha_{IMF}=(D/H)_{measured}/(D/H_{recommended})$.

Table 8. Average ratios of $^{1}H^{-}/^{18}O^{-}$ or $^{16}O^{1}H^{-}/^{18}O^{-}$ of the standards carried out in different analysis sessions.

Session[#]	1		2		3		4	
Sample	$^{1}H^{-}/^{18}O^{-a}$	2SD[b]	$^{1}H^{-}/^{18}O^{-a}$	2SD[b]	$^{1}H^{-}/^{18}O^{-a}$	2SD[b]	$^{1}H^{-}/^{18}O^{-a}$	2SD[b]
MORB	2.20E-01	2.20E-02	2.17E-01	2.82E-02	1.97E-01	3.94E-02	2.03E-01	7.71E-02
DAP	3.27E-02	1.89E-02	4.76E-02	2.05E-02	2.98E-02	7.74E-03	3.55E-02	3.55E-03
KOV			7.67E-01	6.14E-02	6.84E-01	4.42E-02	6.98E-01	3.76E-02

Table 8 (continued)

Session	5		6		7	
Sample	$^{1}H^{-}/^{18}O^{-a}$	2SD[b]	$^{1}H^{-}/^{18}O^{-a}$	2SD[b]	$^{16}O^{1}H^{-}/^{18}O^{-a}$	2SD[b]
MORB	2.05E-01	6.15E-02	1.84E-01	1.39E-02	1.78E-01	4.95E-02
DAP	2.93E-02	9.63E-03	3.08E-02	3.69E-03	1.59E-01	1.22E-02
KOV	6.86E-01	2.44E-02	6.87E-01	1.53E-02	3.63E+00	6.79E-02
1833-1	1.54E+00	1.22E-01			2.08E+00	9.43E-02
1833-11	8.81E-01	7.24E-02			1.03E+00	1.06E-01
519-4-1	1.33E-01	3.01E-02			1.85E-01	2.19E-03
ND 70-01	7.00E-01	5.39E-02			9.40E-01	9.47E-02

[#]Sessions 1 and 2 in the peak jump isotope mode; sessions 3-6 in the multicollection isotope mode; session 7 in the multicollection element mode.

[a]Average of the analyses carried out within single session;

[b]Standard deviation.

Table 9. Parameters of the calibration curves for various analysis mode, with $[^{1}H^{-}/^{18}O^{-}]=\alpha \times [H_2O]+ \beta$.

Session*	Date	α[a]	2SD[b]	2SD[c] (%)	β	2SD[b]	α[a]	2SD[b]	2SD[c] (%)
Peak jump isotope mode									
2	2011.10.24	0.732	0.057	7.8	0.060	0.021	0.790	0.050	6.4
2	2011.10.25	0.705	0.107	15.1	0.063	0.004	0.743	0.019	2.5
2	2011.10.26	0.731	0.030	4.1	0.054	0.012	0.756	0.023	3.0
2	2011.10.29	0.773	0.011	1.4	0.035	0.004	0.778	0.020	2.6
2	2011.10.30	0.801	0.016	2.0	0.034	0.007	0.797	0.006	0.7
2	2011.10.31	0.799	0.052	6.5	0.042	0.021	0.788	0.015	1.9
2	2011.11.01	0.818	0.010	1.2	0.046	0.003	0.827	0.008	1.0
2	2011.11.02	0.801	0.019	2.3	0.046	0.006	0.810	0.011	1.4
	Average	*0.770*	*0.084*	*10.9*	*0.048*	*0.022*	*0.786*	*0.054*	*6.9*
Multicollection isotope mode									
3	2012.04.19	0.742	0.009	1.2	-0.008	0.003	0.736	0.011	1.6
3	2012.04.20	0.694	0.021	3.0	-0.002	0.009	0.692	0.009	1.3
3	2012.04.23	0.693	0.001	0.2	0.001	0.000	0.707	0.036	5.1
3	2012.04.24	0.670	0.035	5.2	0.003	0.015	0.675	0.018	2.6
3	2012.04.25	0.687	0.013	1.9	-0.007	0.005	0.685	0.025	3.7
3	2012.04.26	0.686	0.001	0.2	-0.005	0.000	0.681	0.006	0.9
3	2012.04.27	0.745	0.010	1.3	-0.012	0.004	0.737	0.020	2.6
3	2012.04.28	0.706	0.032	4.5	-0.003	0.014	0.710	0.020	2.8
	Average	*0.703*	*0.054*	*7.7*	*-0.004*	*0.010*	*0.703*	*0.048*	*6.9*
4	2012.12.14	0.690	0.004	0.5	0.003	0.001	0.704	0.013	1.9
4	2012.12.15	0.739	0.014	1.8	0.002	0.005	0.746	0.017	2.3
4	2012.12.17	0.734	0.010	1.3	-0.003	0.004	0.713	0.030	4.1
4	2012.12.18	0.699	0.011	1.6	0.002	0.004	0.701	0.010	1.4
4	2012.12.19	0.706	0.011	1.5	0.007	0.003	0.733	0.023	3.1
4	2012.12.20	0.697	0.006	0.8	0.003	0.001	0.750	0.034	4.6
	Average	*0.711*	*0.041*	*5.8*	*0.002*	*0.006*	*0.724*	*0.043*	*6.0*
5	20130827	0.714	0.011	1.5	-0.012	0.008	0.701	0.010	1.4
5	20130828	0.683	0.014	2.0	0.008	0.009	0.692	0.010	1.5
5	20130829	0.682	0.013	1.9	0.007	0.008	0.689	0.010	1.5
5	20130830	0.666	0.035	5.3	0.007	0.023	0.674	0.024	3.5

5	20130831	0.736	0.025	3.3	-0.010	0.022	0.725	0.009	1.3
5	20130905	0.696	0.008	1.2	-0.005	0.005	0.689	0.006	0.9
5	20130906	0.695	0.014	2.0	-0.005	0.010	0.695	0.006	0.8
5	20130907	0.713	0.008	1.2	-0.007	0.007	0.706	0.004	0.6
5	20130908	0.701	0.004	0.6	-0.008	0.003	0.693	0.003	0.5
5	20130909	0.711	0.004	0.6	-0.005	0.003	0.706	0.003	0.5
5	20130910	0.699	0.022	3.2	-0.004	0.018	0.695	0.012	1.8
5	20130912	0.684	0.011	1.6	-0.002	0.006	0.682	0.009	1.3
5	20130913	0.715	0.006	0.9	-0.005	0.004	0.709	0.005	0.7
5	20130914	0.720	0.002	0.3	-0.005	0.001	0.714	0.006	0.8
5	20130915	0.718	0.004	0.6	-0.006	0.002	0.711	0.006	0.8
5	20130916	0.709	0.001	0.2	-0.005	0.001	0.704	0.005	0.7
5	20130920	0.711	0.002	0.3	-0.006	0.001	0.703	0.013	1.8
5	20130921	0.700	0.020	2.8	-0.009	0.015	0.690	0.013	1.8
5	20130923	0.700	0.009	1.3	-0.006	0.007	0.694	0.006	0.9
	Average	*0.703*	*0.033*	*4.7*	*-0.004*	*0.011*	*0.698*	*0.024*	*3.5*
6	20140425	0.708	0.010	1.4	0.003	0.005	0.711	0.008	1.1
6	20140426	0.702	0.013	1.8	0.001	0.004	0.704	0.010	1.5
6	20140427	0.694	0.010	1.5	-0.001	0.006	0.693	0.008	1.1
	Average	*0.701*	*0.013*	*1.9*	*0.001*	*0.004*	*0.703*	*0.019*	*2.6*

[*]Analytical session 2 was carried out in the peak jump isotope mode and sessions 3-6 in the multicollection isotope mode.

[a]Water content calibration curve using apatite standards and glass standards;

[b]Standard deviation of slope and intercept;

[c]Standard deviation percentage of slope;

[d]Similar to a, but the calibration curves were forced to pass through the coordinate origin.

Italic average: averages and standard deviations of all day analyses within the same analytical session.

Table 10. Parameters of the calibration curves for multicollection element mode, with $[^{16}O^{1}H^{-}/^{18}O^{-}]=\alpha \times [H_2O]+ \beta$.

Mineral	Date	α^a	2SD[b]	2SD[c] (%)	β^a	2SD[b]	α^d	2SD[b]	2SD[c] (%)
Apatite	20140504	3.691	0.029	0.8	-0.002	0.015	3.689	0.023	0.6
	20140505	3.732	0.029	0.8	-0.013	0.016	3.718	0.024	0.7
	20140507	3.688	0.026	0.7	0.004	0.015	3.692	0.021	0.6
	20140516	3.819	0.063	1.6	-0.010	0.015	3.809	0.047	1.2
	Average	*3.733*	*0.122*	*3.3*	*-0.005*	*0.016*	*3.727*	*0.112*	*3.0*
Glass	20140506	0.848	0.013	1.5	0.002	0.012	0.849	0.010	1.2
	20140515	0.872	0.028	3.2	0.044	0.036	0.898	0.022	2.4
	20140516	0.904	0.032	3.5	-0.023	0.037	0.889	0.022	2.4
	20140531	0.839	0.023	2.7	0.026	0.026	0.855	0.017	2.0
	Average	*0.866*	*0.058*	*6.8*	*0.012*	*0.059*	*0.873*	*0.049*	*5.6*

[a]Water content calibration curve using apatite standards or glass standards;

[b]Standard deviation of slope and intercept;

[c]Standard deviation percentage of slope;

[d]Similar to [a], but the calibration curves were forced to pass through the coordinate origin.

Italic average: averages and standard deviations of all analyses within the same analytical session.

Table 11. Calibration curves parameters in multicollection isotope mode using apatite and silicate glass individually.

Mode	Mineral	α^a	2SD[b]	2SD[c] (%)	β^a	2SD[b]	α^d	2SD[b]	2SD[c] (%)
1	Apatite	0.702	0.009	1.2	-0.002	0.005	0.700	0.006	0.9
1	Glass	0.714	0.034	4.7	0.009	0.024	0.723	0.021	2.9

Mode: 1—multicollection isotope mode;

[a]Water content calibration curve using apatite standards or glass standards;

[b]Standard deviation of slope and intercept;

[c]Standard deviation percentage of slope;

[d]Similar to [a], but the calibration curves were forced to pass through the coordinate origin.

Measurements of water content and D/H ratio in apatite and silicate glasses using NanoSIMS 50L

Sen Hu, Yangting Lin*, Jianchao Zhang, Jialong Hao, Wei Yang, Liwei Deng

Key Laboratory of Earth and Planetary Physics, Institute of Geology and Geophysics, Chinese Academy of Sciences, Beijing 100029, China

*Corresponding author, e-mail: linyt@mail.iggcas.ac.cn, Telephone: 0086-10-82998413, Fax: 0086-10-62010846.

Submitted to JAAS (2014)

Abstract: 329 words

Text: ~ 5000 words

Figures: 6

Tables: 11

Abstract

Water plays an important role during evolution of the Earth, Mars, Moon and other planets, with H isotopes used as a crucial tracer for fractionation processes and water reservoirs. In order to accurately and precisely measure water contents and D/H ratios of apatite and silicate glass with high lateral resolution, we carried out a long term measurements with NanoSIMS 50L, with special consideration for H background, calibration of water content and instrumental mass fractionation. A detection limit <10 ppm of water content has been achieved mainly by reducing the level of H background, via improving vacuum and using high primary beam current up to 1 nA and blanking technique.

The measurements were carried out in three modes of detector configuration. In multicollection isotope mode, all $^{1}H^{-}$, $^{2}D^{-}$, $^{12}C^{-}$ and $^{18}O^{-}$ were measured simultaneously. Apatite and silicate glasses with water contents of <1.2 wt% were plotted on a same water content calibration curve with a slope of 0.704±0.037 (2SD). In peak jump isotope mode, $^{1}H^{-}$, $^{2}D^{-}$and $^{12}C^{-}$ were first measured simultaneously at a magnetic field BF1, and then $^{18}O^{-}$ and other elements if needed at BF2 by switching the magnet field. In this mode, apatite and MORB glass standards also share a same water content calibration curve with a slightly higher slope (0.786±0.054, 2SD) relative to that of the multicollection isotope mode. In these two isotope modes, apatite and silicate glass standards have similar instrumental mass fractionation of H isotopes within the analytical uncertainty (45 ‰, 2SD) and similar precisions on water contents, however, the peak jump isotope mode can determine the volatile elements contents and chlorine isotopes. In multicollection element mode, $^{16}O^{1}H^{-}$ (for water content) and $^{18}O^{-}$ were measured simultaneously, accompanied usually by other volatile elements. The slope of water content calibration curve of apatite (3.727±0.112, 2SD) significantly differs from that of silicate glass (0.873±0.049, 2SD). Multicollection element mode can only determine the water and volatile elements contents with two times higher sensitivity than that of two isotope modes.

Keywords: water content, hydrogen isotopes, NanoSIMS, apatite, silicate glasses

1. Introduction

Hydrogen is the most abundant element in our solar system [1]. Meanwhile, hydrogen is also the lightest element and hence has largest mass-dependent fractionation effects in physical and chemical processes, with an extremely wide range of D/H ratios from $(21\pm5)\times10^{-6}$ in protosolar [1, 2], $(4600\pm500)\times10^{-6}$ in interstellar dust particles (IDPs) [3], to $(6000\pm200)\times10^{-6}$ in the atmosphere of Venus [4]. In rocks (terrestrial and extraterrestrial), hydrogen usually occurs as crystallographic water (OH^-); the water content is a key physical property of rocks and has a significant effect on melting of silicates. Apatite is an important and common water-bearing mineral in the Earth, the Moon and other planets. Melt inclusions in early deposited minerals, e.g. olivine, orthopyroxene and chromite, captured the parental magmas, although their compositions may have been changed during eruption of the magmas. Both apatite and melt inclusions are suitable samples for analysis of water contents and H isotopes.

Infrared micro-spectrometry is a traditional method of determining water content in minerals [5], which has a spatial resolution of ~20 μm and a detection limit of <10 ppm. However, infrared spectra contain no information of hydrogen isotopes, and they are strongly related with crystallographic orientation. Secondary Ion Mass Spectrometry (SIMS) has become more common for in-situ analysis of water content, with a unique advantage of hydrogen isotope analysis. IMS f series and IMS 1270/80 are commonly used to determine water contents and hydrogen isotopic compositions, which usually have a H background of 5~30 ppm and a beam size of 10-40 μm [6-9]. Although IMS f series and IMS 1270/80 can measure the water content and hydrogen isotope within a 5×5 μm^2 region via applying a field aperture, it will also sputter away the outer region up to 10-40 μm in diameter depended on the primary beam size. This specific technique has limited applications and hard to be applied to conduct compositional profiles across melt inclusions or mineral crystals with diameter smaller than 50 μm. Recently, NanoSIMS was used to analyze water/volatile element

contents of melt inclusions with an advantage of high lateral resolution. Saal et al. (2008) [10] used NanoSIMS to measure water, F, S and Cl contents of lunar volcanic glasses with 800 nm primary beam @3 nA to raster 12×12 μm area and collect the secondary ions in the center of 4.5×4.5 μm region and found these components were zoned. The precision of water content was around 15 % (2σ) and the H background was around 13 ppm estimated on synthetic forsterite (<0.4 ppm H_2O) under 3×10^{-10} tor in the analysis chamber. Barnes et al. (2013) [11] used a 250 pA primary beam current to analyze water contents and H isotopic compositions of lunar apatite using NanoSIMS with raster size of 10×10 μm and collecting the secondary ions in the center 5×5 μm region. H background was 20-110 ppm estimated on the intercept of the water content calibration curve under a vacuum of 1×10^{-9} tor and H isotope precision was 40-80 ‰ (2σ). By mapping H distribution in olivine, Mosenfelder et al. (2011) [12] found H-rich sub-micro inclusions, which explains the discrepancy between the IMS 5f and FTIR measurements. NanoSIMS was also used to map H isotopic compositions of fine-grained mixtures of organic matter and phyllosilicates [13]. Hauri et al. (2011) [14] compared data achieved by both mapping method and spot analysis, and the results were consistent with each other. In addition, NanoSIMS images are very helpful to assess contamination of epoxy that filled in fractures and cleavages of apatite and other minerals.

Different from an illumination analysis mode of the IMS f series and IMS 1270/80 [6, 9, 15], NanoSIMS rasters the primary beam over analysis areas, with potential contamination due to H re-depositing on the surface. Stephant et al., (2014) [16] estimated H background via measuring the DR15-2-5 basaltic glass (0.2581 wt. % H_2O) using NanoSIMS mapping method. They found that the H background highly depended on the vacuum of the analysis chamber and the intensity of the primary beam current. In addition, the yield rate of $^{1}H^{-}$ (or $^{16}O^{1}H^{-}$) relative to $^{30}Si^{-}$ (or $^{18}O^{-}$) of the same H-bearing standards was also related with the intensity of the primary beam current [16]. The H background determined by previous researchers using NanoSIMS

varied from 10-110 ppm with analysis vacuum range from 3×10^{-10} tor to 1×10^{-9} tor [10-12].

In this work, we carried out systematic measurements on H background, under various operating conditions including vacuum of the analysis chamber, intensity of the primary beam current, dwell time and application of blanking technique. The water content calibration curves and instrumental mass fractionation (IMF) of H isotopes were determined with apatite and silicate glasses standards using NanoSIMS 50L under three different analytical modes.

2. Standard Samples and Experiments

Eight mineral and glass standards were used in this study, including two apatite (Kovdor and Durango), one olivine (San Carlos), one MORB glass (SWIFT), and four basaltic glasses (1833-1, 1833-11, 519-4-1, and ND 70-01). These samples cover a range of water contents up to 2.43 wt. %, and three of them have known D/H ratios. The water contents and H isotopic compositions of these standards are listed in Table 1.

Table 1. Apatite and silicate glass standards used in this work.

All standard samples were imbedded in Crystalbond resin, then grinded and polished. After polishing, the samples were cleaned in acetone with ultrasonic, to remove Crystalbond resin. This cleaning process was repeated 5 times in a period of 24 h to make sure Crystalbond resin has completely been removed. The resin-free polished standard samples were then dried at 105 ºC in an oven for 12 h, and finally impressed into indium disks. After coated with gold, the samples were loaded and stored in the vessel chamber of NanoSIMS 50L under a high vacuum condition ($<5\times10^{-9}$ tor) at least a week before measurement.

All of the measurements were carried out with a NanoSIMS 50L at Beijing

NanoSIMS Lab, the Institute of Geology and Geophysics, Chinese Academy of Sciences (IGGCAS). A Cs^+ primary beam of ~0.5 nA and ~1 μm in diameter with an impact energy of 16 kV was applied in most analyses, except for measurements of H background related with the intensity of the primary beam. Surface charge was compensated with an electron gun (E-gun). Electron multipliers (EMs) were used to count the secondary ions. The dead time (44 ns) of EMs was corrected, and the noise of EMs ($<10^{-2}$ cps) was ignored.

Three analysis modes, including multicollection isotope mode, peak jump isotope mode and multicollection element mode, were applied in this work, which meet various applications (Table 2).

In multicollection isotope mode, secondary ions of $^1H^-$, $^2D^-$, $^{12}C^-$ and $^{18}O^-$ (Table 2) were collected simultaneously. However, the location of the EM to collect $^1H^-$ in this mode (~161 mm) is much lower than that of peak jump isotope mode (~198 mm) (Table 2), which will result in the tilt angles of $^1H^-$ is significant higher than that of larger radius [22]. The deflector and ESA in front of the EM#1 have to be tuned to maximize the $^1H^-$ counts. $^{12}C^-$ was used as a contamination index and $^{18}O^-$ was used as an internal reference for water content calibration. A 0.5 nA primary beam current was used for analysis. Each analysis was pre-sputtered by 15×15 μm^2 with a beam current of 2 nA to eliminate surface contamination. Each analysis has 10 blocks by 50 cycles. Each cycle contains 64×64 pixels with default counting time of 132 μs for each pixel. The counting time for each analysis is ~ 8 minutes. A mass resolving power (MRP) of 1800-2000 and ~5000 (M/ΔM, 10 % definition) is sufficient to resolve $^2D^-$ from the interference of $^1H_2^-$ and $^{18}O^-$ from the interference of $^{17}O\ ^1H^-$, respectively. In this mode, the yield rate of $^1H^-$ is ~63 cps/nA/ppm on DAP and ~80 cps/nA/ppm on MORB, and the counting rates of $^{18}O^-$ on both samples are ~600,000 cps (counts per second). Water contents and hydrogen isotopic compositions can be measured in this mode.

In peak jump isotope mode, secondary ions of $^1H^-$, $^2D^-$ and $^{12}C^-$ were counted

simultaneously at magnetic field BF1, then switch the magnet to collect $^{18}O^-$ (Table 2). Other volatile elements, like $^{19}F^-$, $^{31}P^-$, $^{32}S^-$, $^{35}Cl^-$, and $^{37}Cl^-$ secondary ions can also be collected if needed. The instrument setup was identical with multicollection isotope mode except the positions of detectors. The counting time for each analysis is ~20 minutes. The yield rate of $^1H^-$ is ~84 cps/nA/ppm on DAP and ~120 cps/nA/ppm on MORB, and the counting rates of $^{18}O^-$ is same as multicollection isotope mode. Water content, hydrogen isotopic composition, chlorine isotope and other volatile element content can be measured in this mode.

In multicollection element mode, secondary ions of $^{16}O\,^1H^-$, $^{18}O^-$ (Table 2) were collected simultaneously. Other volatile elements, like $^{19}F^-$, $^{31}P^-$, $^{32}S^-$, and $^{37}Cl^-$ secondary ions can also be collected if needed. A 0.5 nA primary beam current was used for analysis. Each analysis was pre-sputtered by 15×15 μm^2 with a beam current of 2 nA to eliminate surface contamination. Each analysis has 10 blocks by 50 cycles. Each cycle contains 64×64 pixels with default counting time of 132 μs for each pixel. The counting time for each analysis is ~ 8 minutes. A mass resolution of 6,000 is needed to resolve $^{16}O\,^1H^-$ from the interference of $^{17}O^-$. Meanwhile, $^{16}O\,^1H^-$ instead of $^1H^-$ was used to determine the water content, as the former has around 2 times higher yield rate under Cs^+ source with same instrument setup [23, 24], different with the upper two modes. In this mode, the counting rate of $^{18}O^-$ is around 150,000 cps. The yield rate of $^{16}O^1H^-$ on DAP, KOV and 1833-1 are around 59 cps/nA/ppm, 92 cps/nA/ppm and 24 cps/nA/ppm, respectively. This mode was only used to measure the volatile element content, in regardless of hydrogen isotope.

Table 2. Detector setup for water content and hydrogen isotope analyses using NanoSIMS 50L.

Because of high counting rates of $^1H^-$, $^{16}O^1H^-$ and $^{18}O^-$, the pulse height distribution (PHD) on these EMs were checked and adjusted every 8 hours, in order to

reduce the aging effect, which could increase $\delta^{34}S$ by 20 ‰ with PHD_{max} varied from 170 mV to 280 mV [25]. E-gun may sputter less than 50 cps of $^{1}H^{-}$ ions and much less $^{16}O^{1}H^{-}$ ions (<1 cps). Both ions sputtered by E-gun can be negligible.

3. Results and discussion

3.1 Effects on H background

3.1.1 Blanking

The multicollection isotope mode was used for H background test with analytical conditions changed for individual consideration. H background must be studied on anhydrous minerals or materials. Re-deposition of sputtered materials is a main source of surface contamination of H, and it can be recognized as a high intensity of H^{-} (or OH^{-}) along the margins of the analysis area. This surface can be eliminated using blanking technique of NanoSIMS 50L, which integrates signals only from the pre-defined inner region of the scanning area. In order to assess blanking effect on the H background, three samples (Ol, DAP and KOV) with different water contents were measured with blanking percentages varying from 0 % to 92 %. A 0.5 nA primary beam current was used for analysis. Each analysis was pre-sputtered by 15×15 μm^2 with a beam current of 2 nA to eliminate surface contamination with 3 minutes. Each analysis has 10 blocks by 50 cycles. Each cycle contains 64×64 pixels with default counting time of 132 μs for each pixel. The results are listed in Table 3 and plotted in Fig. 1. The $^{1}H^{-}/^{18}O^{-}$ ratios of DAP and KOV are independent on the blanking percentages. In contrast, the $^{1}H^{-}/^{18}O^{-}$ ratios of the H-poor Ol standard decrease significantly with the blanking percentage increasing up to 50 %, and reached a constant ratio of ~1.4E-3 afterward (Fig. 1e and Table 3). These results indicate significant surface contamination during analyzing H-poor samples without sufficiently blanking the outer margins of analysis area. However, blanking technique

may be not necessary for analysis of samples with water contents of >250 ppm. Because of cutting signals, the statistical uncertainty of D/H ratios could significantly become larger with higher blanking percentage (Fig 1b and 1d). We recommend a 50 % blanking percentage for routine measurements.

Fig. 1 Blanking effect on Ol, DAP and KOV

Table 3. Measurements of the standards with various blanking percents.

3.1.2 Vacuum of the analysis chamber

In order to assess H background contributed by vacuum of the analysis chamber, $^{1}H^{-}$ on anhydrous silicon wafer and high temperature synthetic sapphire were counted under various levels of vacuum of the analysis chamber via booting the titanium sublimation pump every 30 min on an epoxy prepared sample. The analysis area was set to 10×10 μm^2 with 50 % blanking and the other analytical conditions were same as blanking test. The hydrogen counting rates (H_{cps}) on both silicon wafer and sapphire are correlated with the vacuum levels (Fig. 2 and Table 4). With the vacuum better than 5E-10 tor (E-gun on), the H_{cps} are less than ~500 cps, corresponding to ~10 ppm (500 cps of H on silicon wafer over 600,000 cps of O) in water contents. If the vacuum becomes poor to 1E-9 tor, the H_{cps} on silicon wafer can reach up to ~20,000 cps (Fig. 2 and Table 4), or a background of ~330 ppm H_2O (20,000 cps of H on silicon wafer over 600,000 cps of O). This measurement confirms previous reported correlation between H background and vacuum of analysis chamber [6]. Since degassing of epoxy used to prepare sections has a main contribution to poor vacuum condition, high vacuum epoxy should be used in sample preparing, and its mass should be reduced as less as possible.

Fig. 2 Counting rate of H vs the vacuum of the analysis chamber

Table 4. $^{1}H^{-}$ counting rate of anhydrous silicon wafer and sapphire under various conditions of vacuum in the analysis chamber.

3.1.3 Intensity of primary beam current

The $^{1}H^{-}$ counts acquired on anhydrous minerals or materials can be divided into two parts, one is the mainly contribution from the surface re-condensation and the other is much weak sputtered from anhydrous sample. The level of H background relative to H counting rates of samples might be related to the intensity of the primary beam, if both signals have different response to the latter. A relatively lower H background may be achieved via applying a high intensity of the primary beam to increase the percentage of H counts from the sample over the surface contamination, equivalent to decrease the H background. In order to test this possibility, the San Carlos olivine was measured using various intensities of the primary beam (FCo) ranging from 1 pA to 1 nA (Fig. 3 and Table 5). Higher current was not tested as constrained by the maximum count capacity of EM. The other analytical conditions were same as blanking test. The measurements were plotted in Fig. 3, which shows a negatively correlation between $^{1}H^{-}/^{18}O^{-}$ and primary beam current in a log scale. Figure 3 indicates the H background can be further decreased via using a higher primary beam current, probably higher current can sputter more $^{1}H^{-}$ signals from the sample relative to background.

Fig. 3 FCo vs $^{1}H^{-}/^{18}O^{-}$ ratio on San Carlos olivine

Table 5. Measurements of San Carlos olivine with various primary beam current.

3.1.4 Dwell time

The dwell time on each pixel of the analysis area would be related with H

background. If the scanning speed of analysis is faster than the rate of H re-deposition, H background can be further decreased. In order to test this possibility, the analyses were carried out on San Carlos olivine. Each analysis has 10 blocks, and each block consists of 160 to 1 cycles of 64 pixel × 64 pixel, corresponding to a dwell time varying from 16 μs/px to 2,640 μs/px, keeping a same total integrating time of 104.8 seconds. The other analytical conditions are same as blanking test. The average $^{1}H^{-}/^{18}O^{-}$ ratios on San Carlos olivine are nearly constant around 7.2E-4 within reproducibility of 1.23E-04 with dwell time varied from 16 μs/px to 2640 μs/px. There is no significant correlation between the $^{1}H^{-}/^{18}O^{-}$ ratios and the dwell time, although the range of $^{1}H^{-}/^{18}O^{-}$ ratios (statistical errors) intends to be smaller for higher dwell time (Fig. 4 and Table 6).

Fig. 4 Dwell time on San Carlos olivine measurements.

Table 6. Measurements of San Carlos olivine with different dwell time.

3.1.5 Optimizing analysis conditions

After blanking, vacuum, primary beam intensity and dwell time tests, the analysis conditions were optimized. A 0.5 nA primary beam current was used for analysis. Each analysis area was pre-sputtered for 3 minutes by rastering 15×15 μm^2 with a beam current of 2 nA to eliminate surface contamination and achieve stable yield rates of the secondary ions. The analysis area was normally set to 10×10 μm^2. Each analysis contains 10 blocks by 50 cycles. Each cycle contains 64×64 pixels with default counting time of 132 μs for each pixel. Fifty percent of the outmost analysis area was blanked in order to eliminate possible contamination from the surroundings. The standard samples were loaded into vessel chamber before a week of analyses. The vacuum of analysis chamber can reach to lower than 5×10^{-10} tor with the H

background of ~10 ppm. The H background was monitored on anhydrous olivine, silicon wafer and sapphire.

3.2 Instrumental mass fractionation

D/H ratios of Kovdor apatite standard and MORB glass standard have been analyzed in two isotope modes within a period of 48 months, in order to assess the instrument mass fractionation (IMF=1000×[$D/H_m/D/H_t$-1], where D/H_m is the measured result and D/H_t is the recommended value). The results are summarized in Table 7 and plotted in Fig. 5. IMF depended on the analytical sessions and varied from 8±48 ‰ – 188±66 ‰ in peak jump isotope mode and 51±51 ‰ – 195±59 ‰ in multicollection isotope mode, nearly identical within analytical uncertainties (Table 7). IMF of Kovdor apatite and MORB glass varied from 10-182 ‰ and 8-195 ‰, respectively (Table 7). It is noticed that the apatite standard and MORB glass standard have the same IMF within the analytical uncertainties (with a difference <45 ‰), regardless of variation among analytical sessions (Fig. 5 and Table 7), indicating apatite and basaltic glasses don't have matrix effect for hydrogen isotopes. The hydrogen isotope precision of Kovdor apatite is less than 38 ‰ (all uncertainties used in the paper are 2SD), significant lower than that of MORB glass (45-66 ‰) as its higher water content with more $^2D^-$ counts (Table 7).

Fig. 5 Instrument mass fractionation (IMF) of hydrogen isotope on MORB glass and Kovdor apatite in all analytical sessions.

Table 7. Instrument mass fractionation (IMF) and hydrogen isotope correction coefficient (α_{IMF}) of MORB glass and Kovdor apatite.

3.3 Calibration on water content

The water contents were determined from the $^{1}H^{-}$ and $^{16}O\,^{1}H^{-}$ intensities relative to $^{18}O^{-}$ using the calibration curves. In order to establish the calibration curves, the apatite and silicate glass standards have been measured in three analysis modes, and the results are summarized in Table 8-10 and plotted in Fig. 6.

3.3.1 Multicollection isotope mode

Firstly, the water content calibration curves ($[^{1}H^{-}/^{18}O^{-}] = \alpha \times [H_2O] + \beta$) were determined by apatite and glasses standards, and the H background was not subtracted. The results are listed in the first fragment of Table 9. The α values of 4 multicollection sessions (sessions 3-6) in isotope mode are nearly identical (0.703±0.054, 0.711±0.041, 0.703±0.033 and 0.701±0.013). The β values of the 4 multicollection sessions in isotope mode are very small (-0.004±0.010, 0.002±0.006, -0.004±0.011 and 0.001±0.004), mainly due to uncertainty in the linear regression instead of H background that is <10 ppm H_2O.

Secondarily, all analyses have been subtracted by the H backgrounds (~10 ppm for all sessions, comparable with the intercept of water content calibration curves without H background subtracted). The calibration curves were forced to pass through the coordinate origin, in order reduce analytical errors when the curves are extrapolated to very low $^{1}H^{-}/^{18}O^{-}$ ratios. It is noticed that the α values are nearly the same within the uncertainties (<6.9 %) and the apatite and glass standards show a linear correlation (Table 9 and Fig. 6b).

Finally, for comparison with the water calibration curves in multicollection element mode, apatite and glass standards were separated for regress the water content calibration curves in session 5. As 1833-1 contains much higher water than the other standards, it was not used for regression. The α values regressed from apatite and silicate glasses are also identical within analytical uncertainties (0.702±0.009 vs 0.714±0.034 for H background non-subtracted and 0.700±0.006 vs 0.723±0.021 for H background subtracted) (Table 11).

3.3.2 Peak jump isotope mode

Similar with multicollection isotope mode, the α values of peak jump isotope mode is 0.770±0.084 for H background non-subtracted and 0.786±0.054 for H background (~400 ppm as poor analysis vacuum) subtracted. The slope of water content calibration curves in peak jump isotope mode is significant higher than that of multicollection isotope mode, because the EM for H was set at larger radius for the latter (Table 2).

3.3.3 Multicollection element mode

Firstly, similar with multicollection isotope mode, the calibration curves ($[^{16}O^{1}H^{-}/^{18}O^{-}] = \alpha \times [H_2O] + \beta$) were determined by apatite and glasses standards, and the H background was not subtracted. The results are listed in the first fragment of Table 10. The α values of apatite and glasses in element mode are 3.733±0.122 and 0.866±0.058, respectively (Table 10). The corresponding β values are -0.005±0.016 for apatite standards and 0.012±0.059 for glass standards.

Secondary, the calibration curves were forced to pass through the coordinate origin and H background (~10 ppm) subtracted. The α values of apatite and glasses are 3.727±0.112 and 0.873±0.049, respectively, which are same with H background non-subtracted slopes within the uncertainties (Table 10).

Regardless of significant differences in chemical compositions between apatite and basaltic glass, they share a similar calibration curve within analytical uncertainties in all sessions of peak jump and multicollection isotope modes (Fig. 6a and 6b and Table 9 and 11). Whereas, the calibration slopes varied from 0.786±0.054 in peak jump isotope mode to 0.704±0.037 (average of 4 analytical sessions within two years) in the multicollection isotope mode (Fig. 6 and Table 9), probably depending on the radius of EM used to count $^{1}H^{-}$ signals (Table 2). Previous analyses of silicates with different compositions varying from rhyolitic to basaltic have also demonstrated similar matrix effects for low-H_2O samples (<1.5 wt%), although significant matrix effects for samples with water contents > 2 wt% [6]. The basaltic glass 1833-1 contains

the highest water content of 2.43 wt%, and it plots significantly deviated from the linear trend. The similar deviation has also been reported by Hauri et al. (2002) [6]. In multicollection element mode, apatite samples behave completely different from the silicate glass standards, with both plotted on two distinct calibration curves. The slope of water content calibration curves of apatite (3.727±0.112) is significant higher than that of glasses (0.873±0.049) in the multicollection element mode (Fig. 6c and Table 10). Furthermore, the highest water contents basaltic glass 1833-1 showed no deviation within uncertainty along the linear trend of the calibration curve. Those effects would be induced by the difference of water form in the mineral and glasses. The major water form is hydroxyl in apatite based on the chemical formula. For comparison, the major water form of glasses is hydroxyl and water molecular based on the FTIR analyses [26, 27]. When using Cs^+ primary beam to sputter the $^{16}O^1H^-$ secondary ions, $^{16}O^1H^-$ is more easily sputtered from apatite than glasses, as water molecular needs more energy to break the chemical bond and capture an electron to form $^{16}O^1H^-$ ions. In contrast, when using $^1H^-/^{18}O^-$ to measure water contents, all of the water bearing species (OH^- in apatite, OH^- and H_2O molecular in glasses) would be transformed into $^1H^-$.

The errors of water content calibration curves in peak jump isotope mode are 10.9 % for H background non-subtracted and 6.9 % for H background subtracted (Table 9). In contrast, the errors of water content calibration curves within 4 analytical sessions in multicollection isotope mode are 1.9-7.7 % for H background non-subtracted and 2.6-6.9 % for H background subtracted (Table 9). It seems that errors in peak jump isotope mode are slightly higher than that in multicollection isotope mode (Table 9). In multicollection element mode, the error of water content calibration curve of apatite (<3.3 %) is significantly lower than that of silicate glasses (<6.8 %) (Table 10). Anyway, the maximum uncertainty of the slopes of the water content calibration curves in all analytical sessions is lower than 6.9 % for H background subtracted (Table 9 and 10).

Fig. 6 Water content calibration curves between all analytical sessions.

Tabel 8. Summary of $^{1}H^{-}/^{18}O^{-}$ or $^{16}O^{1}H^{-}/^{18}O^{-}$ ratios within single session.

Table 9. Parameters of the calibration curves for peak jump isotope mode and multicollection isotope mode, with $[^{1}H^{-}/^{18}O^{-}]=\alpha \times [H_2O]+ \beta$.

Table 10. Parameters of the calibration curves for multicollection element mode, with $[^{16}O^{1}H^{-}/^{18}O^{-}]=\alpha \times [H_2O]+ \beta$.

Table 11. Comparison of calibration curves parameters using apatite and silicate glasses individually in multicollection isotope mode.

3.3.4 Accuracy

In order to assess the analytical errors, the measurements of the apatite and glass standards were treated as unknown samples using the calibration curves of individual analytical sessions. The differences between the average results and the recommended values are <2 % for Kovdor apatite, <13 % for Durango apatite (except for 27 % in October 2011 session), <11 % for MORB glass, 3 % for ND 70-01, 5 % for 519, 2 % for 1833-11 and 12 % for 1833-1 (Table S1 and S2).

3.4 Potential application of the three analytical modes

The three analytical modes have different applications. Multicollection isotope mode is fit for analyzing Martian samples to study the water contents and hydrogen

isotopes with $^{12}C^-$ index removing the terrestrial contamination. At BF2 in peak jump isotope mode, it can collect another four element/isotopes (F, S, ^{35}Cl and ^{37}Cl) with idle EMs, so it can determine water contents, hydrogen isotopes, volatile element contents and/or Cl isotopes simultaneously, which can be used to analyze lunar apatite, melt inclusions and volcanic glasses to study volatile element contents in lunar interior and constrain their origin. Compared with multicollection isotope mode, it takes a longer counting time with comparable precisions for water contents and hydrogen isotopes. Multicollection element mode can determine volatile element contents and Cl isotopes without hydrogen isotopes. However, this mode has higher sensitivity compared with the two isotope modes, because yield rate of $^{16}O^1H^-$ is two times higher than $^1H^-$ under same instrument setup. It fits for analyzing the volatile element contents and Cl isotopes, *e.g.* apatite and melt inclusions from Earth interior. However, water content in this mode has significant matrix effect between apatite and silicate glasses.

4. Summary

H background is closely correlated with the analysis vacuum. However, blanking and primary beam current will also affect the H background. Under 3×E-10 tor, the H background is around 10 ppm under 0.5 nA primary beam current, 50% blanking and 132 μs/pixel dwell time, determined on nominal anhydrous materials San Carlos olivine, silicon wafer and sapphire. Blanking technique can be used to decrease the surrounding contamination of the analysis targets when measuring very low water content samples. High beam current can improve the ratio of H signals to H background. Dwell time on each pixel doesn't affect the H background in the ranges of 16 μs/px to 2,640 μs/px.

Our long period measurement up to 48 months demonstrates that the apatite and MORB glass showed same instrument mass fractionation of H isotopes within the analyses uncertainties (45 ‰). Furthermore, both apatite and silicate glass standards

share a similar calibration curve in case the water contents were determined from relative intensity of $^{1}H^{-}$. In contrast, the calibration curve using relative intensity of $^{16}O^{1}H^{-}$ is very dependent on minerals, with a slope of the curve 0.786±0.054 for glasses standards and another slope of 3.727±0.112 for apatite standards.

The three analysis modes can satisfy various applications. Multicollection isotope mode is best fit for measuring Martian samples, as C can be used for monitoring the contamination in apatite. Peak jump isotope mode is best fit for measuring lunar apatite to constrain its origin of water, as it can measure water content, H isotope, Cl isotope and volatile element content simultaneously. Multicollection element mode is fit for measuring the water contents without H isotope. Using this method, we successfully measured the water contents and hydrogen isotope of apatite and magmatic inclusions in Martian meteorite GRV 020090 [28].

5. Acknowledgements

The constructive reviews by two anonymous referees have significantly improved this paper. The authors are grateful to Fuyuan Wu, David Chew, Francois Robert and Erik Hauri for providing the standard samples. This study was financially supported by the National Natural Science Foundation of China (41273077, 41221002 and 41103031).

6. References

1. E. Anders and M. Ebihara, *Geochimica Et Cosmochimica Acta*, 1982. **46**, 2363-2380.
2. J. Geiss and G. Gloeckler, *Space Science Reviews*, 1998. **84**, 239-250.
3. J. Duprat, E. Dobrică, C. Engrand, J. Aléon, Y. Marrocchi, S. Mostefaoui, A. Meibom, H. Leroux, J.-N. Rouzaud, M. Gounelle, and F. Robert, *Science*, 2010. **328**, 742-745.
4. T. Donahue, J. Hoffman, R. Hodges, and A. Watson, *Science*, 1982. **216**, 630-633.
5. G.R. Rossman, *Reviews in Mineralogy and Geochemistry*, 2006. **62**, 1-28.

6. E. Hauri, J. Wang, J.E. Dixon, P.L. King, C. Mandeville, and S. Newman, *Chemical Geology*, 2002. **183**, 99-114.
7. K. Koga, E. Hauri, M. Hirschmann, and D. Bell, *Geochemistry Geophysics Geosystems*, 2003. **4**, 1019.
8. N. Sugiura and H. Hoshino, *Meteoritics & Planetary Science*, 2000. **35**, 373-380.
9. J.P. Greenwood, S. Itoh, N. Sakamoto, E.P. Vicenzi, and H. Yurimoto, *Geophysical Research Letters*, 2008. **35**.
10. A.E. Saal, E.H. Hauri, M.L. Cascio, J.A. Van Orman, M.C. Rutherford, and R.F. Cooper, *Nature*, 2008. **454**, 192-195.
11. J.J. Barnes, I.A. Franchi, M. Anand, R. Tartèse, N.A. Starkey, M. Koike, Y. Sano, and S.S. Russell, *Chemical Geology*, 2013. **337–338**, 48-55.
12. J.L. Mosenfelder, M. Le Voyer, G.R. Rossman, Y. Guan, D.R. Bell, P.D. Asimow, and J.M. Eiler, *American Mineralogist*, 2011. **96**, 1725-1741.
13. L. Piani, L. Remusat, and F.o. Robert, *Analytical Chemistry*, 2012. **84**, 10199-10206.
14. E.H. Hauri, T. Weinreich, A.E. Saal, M.C. Rutherford, and J.A. Van Orman, *Science*, 2011. **333**, 213-215.
15. J.P. Greenwood, S. Itoh, N. Sakamoto, P. Warren, L. Taylor, and H. Yurimoto, *Nature*, 2011. **4**, 1-4.
16. A. Stephant, L. Remusat, A. Thomen, and F. Robert, *Chemical Geology*, 2014. **380**, 20-26.
17. S.L. Nadeau, S. Epstein, and E. Stolper, *Geochimica Et Cosmochimica Acta*, 1999. **63**, 1837-1851.
18. E. Stolper and S. Newman, *Earth and Planetary Science Letters*, 1994. **121**, 293-325.
19. G. Fine and E. Stolper, *Earth and Planetary Science Letters*, 1986. **76**, 263-278.
20. C. Aubaud, A.C. Withers, M.M. Hirschmann, Y. Guan, L.A. Leshin, S.J. Mackwell, and D.R. Bell, *American Mineralogist*, 2007. **92**, 811-828.
21. J. Hoefs, *Stable Isotope Geochemistry*. 6th ed. 2009: Springer Berlin Heidelberg.
22. F. Hillion, F. Horreard, and F.J. Stadermann, *Recent results and developments on the CAMECA NanoSIMS 50*, in *Poster for SIMS XII*1999: Brussels, Belgium.
23. J.C. Rienstra-Kiracofe, G.S. Tschumper, H.F. Schaefer, S. Nandi, and G.B. Ellison, *Chemical Reviews*, 2002. **102**, 231-282.
24. C.-G. Zhan, J.A. Nichols, and D.A. Dixon, *Journal Name: Journal of Physical Chemistry A, 107(20):4184-4195*, 2003, Medium: X.
25. J. Zhang, Y. Lin, W. Yang, W. Shen, J. Hao, S. Hu, and M. Cao, *Journal of Analytical Atomic Spectrometry*, 2014. **29**, 1934-1943.
26. L. Silver, P. Ihinger, and E. Stolper, *Contributions to Mineralogy and*

Petrology, 1990. **104**, 142-162.
27. E. Stolper, *Contributions to Mineralogy and Petrology*, 1982. **81**, 1-17.
28. S. Hu, Y. Lin, J. Zhang, J. Hao, L. Feng, L. Xu, W. Yang, and J. Yang, *Geochimica et Cosmochimica Acta*, 2014. **140**, 321-333.

Figure caption

Fig.1 Blanking effect on San Carlos olivine (Ol), Durango apatite (DAP) and Kovdor apatite (KOV). The measured $^{1}H^{-}/^{18}O$- ratios of KOV (a) and DAP (c) keep constant with blanking from 0 % to 92 %. The measured D/H ratios of KOV (b) and DAP (d) show increase in uncertainty with blanking increase from 0 % to 92 %. The $^{1}H^{-}/^{18}O^{-}$ ratios of the Ol standard decrease significantly with the blanking percentage increasing up to 50 %, and reached a constant ratio of ~1.4E-3 afterward.

Fig. 2 Counting rate of H vs the vacuum of the analysis chamber. The H_{cps} on anhydrous sapphire and silicon wafer is positively correlated with vacuum of analysis chamber in log scale.

Fig. 3 Intensity of primary beam (FCo) vs $^{1}H^{-}/^{18}O^{-}$ ratio on San Carlos olivine. The measured $^{1}H^{-}/^{18}O^{-}$ ratios on San Carlos olivine are negatively correlated with primary beam intensity (FCo) in log scale.

Fig. 4 Dwell time effect on San Carlos olivine. The average $^{1}H^{-}/^{18}O^{-}$ ratios on San Carlos olivine are nearly constant around 7.2E-4 with dwell time varied from 16 μs/px to 2640 μs/px. There is no significant correlation between $^{1}H^{-}/^{18}O^{-}$ ratios and dwell time.

Fig. 5 Instrumental mass fractionation (IMF) of hydrogen isotope on MORB glass and Kovdor apatite in all analytical sessions. IMF of Kovdor apatite and MORB glass varied from 10-182 ‰ and 8-195 ‰, respectively. Apatite standard and MORB glass standard have the same IMF within the analytical uncertainties (with a difference <45 ‰), regardless variation among analytical sessions. The hydrogen isotope precision of Kovdor apatite is less than 38 ‰, significant lower than that of MORB glass (45-66 ‰).

Fig. 6 Water content calibration curves between all analytical sessions. The apatite and silicate glasses share a same water content calibration curves in multicollection isotope mode and peak jump isotope mode. The slope of water content calibration curve of peak jump isotope mode (0.786) is significant higher than that of multicollection isotope mode (0.704). The water content calibration curve of apatite (3.727) is totally different with that of silicate glasses (0.873) in multicollection element mode.